Energy Storage Materials 16 (2019) 411–418

Contents lists available at ScienceDirect

Energy Storage Materials

journal homepage: www.elsevier.com/locate/ensm

Regulating Li deposition by constructing LiF-rich host for dendrite-free lithium metal anode

Yanxia Yuan[a], Feng Wu[a,b], Ying Bai[a,*], Yu Li[a], Guanghai Chen[a], Zhaohua Wang[a], Chuan Wu[a,b,*]

[a] Beijing Key Laboratory of Environmental Science and Engineering, School of Materials Science & Engineering, Beijing Institute of Technology, Beijing, PR China

[b] Collaborative Innovation Center of Electric Vehicles in Beijing, Beijing 100081, PR China

ARTICLE INFO

Keywords:
Lithium metal anode
LiF-rich host
NH_4HF_2
Dendrite-free

ABSTRACT

Lithium (Li) metal anode is among the most promising anodes due to its high energy density. However, the long-standing issue of Li dendrites growth hinders the practical application of lithium metal batteries (LMBs) in portable electronics and electric vehicles. Engineering a dendrite-free Li metal anode is therefore critical for the development of long-life batteries. Here, an artificial LiF host with cuboid feature is constructed on Li metal surface by a facial one-step reaction of ammonium hydrogen difluoride (NH_4HF_2) with bare Li metal. During cycling, Li grows continuously from the bottom gaps to the top of the LiF host and finally cover the surface of the modified anode. Particularly, with the increasing of cycling capacity, the Li metal tend to deposit into scaly morphology which contributes to a dendrite-free anode. The as-obtained smooth Li anodes enabled stable cycling in working batteries with a low overpotential and a high Coulombic efficiency (CE) of 98.5% at the current density of 1 mA cm^{-2}. This work provides a facile approach to prepare LiF-rich Li anode which paves the way to construct high-energy and safe LMBs.

1. Introduction

Lithium ion batteries (LIBs) have been widely applied in electric vehicles, portable devices, robots and power tools. Though LIBs are now gradually approaching their theoretical limit [1], they still fail to meet the continuously increasing demand for large-scale energy storage systems and power batteries [2–5]. Therefore, to meet the growing demand of stationary or mobile energy storage, some multi-valent rechargeable batteries, owing to their potential high performances originated from multi-electron electrochemical reactions, are being extensively explored [6–8]. Meanwhile on the dependable basis of lithium secondary batteries, Li metal anode is urgently needed to dramatically improve the energy density of state-of-the-art rechargeable batteries owing to its very high theoretical specific capacity (3862 mAh g^{-1}), low gravimetric density (0.53 g cm^{-3}) and the lowest reduction potential (-3.04 V *vs.* standard hydrogen electrode) [9–12]. Nevertheless, the adoption of the LMBs will open up opportunities of using non-lithiated cathode materials such as metal sulfides and oxides, S_8, O_2, CO_2, et al. [13–17] However, several intrinsic obstacles have limited the application of metallic Li, such as the low CE of Li plating/stripping, uncontrolled dendritic deposition on metallic Li surface, the generation of “dead Li” and the side reactions between Li anode and electrolyte [2,18].

Therefore, in recent years, great efforts have been spent into the modification of LMBs. Optimizing the components of electrolytes has been proven to promote the cycle stability of Li anode by influencing the properties of solid electrolyte interphase (SEI) film [19]. Some electrolyte additives, such as water [20], LiF [21], fluoroethylene carbonate (FEC) [22] and $CsPF_6$ [23–25] have been adopted to participate in SEI formation, and thus render a high mechanical strength even after many cycles. Replacing the carbonaceous liquid electrolytes by more stable candidates such as ether-based electrolytes [26], quasi-solid-state [27,28] or solid-state electrolytes [29–36], can also effectively optimize the Li depositional behavior. However, Li^+ tend to deposit on a lumped site to form dendrites, mainly because of the high surface diffusion energy barrier on Li anode. The surface energy and diffusion energy of surface layer significantly influence the Li depositional behavior [37]. The initial nucleation sites also play an important role in the succedent Li depositional morphology [10,38,39]. Thus, more attention should be paid to the features and chemical compositions of the surface layer [40–44]. The surface energy and diffusion barrier of many components have been calculated [45], including layered (LiOH), multivalent (Li_2O, Li_2CO_3), and halide (LiF, LiCl, LiBr, LiI) compounds. The joint density functional theoretical (JDFT) analysis showed that a lithium-halide SEI layer gives rise

* Corresponding author at: Beijing Key Laboratory of Environmental Science and Engineering, School of Materials Science & Engineering, Beijing Institute of Technology, Beijing, PR China.
E-mail addresses: membrane@bit.edu.cn (Y. Bai), chuanwu@bit.edu.cn (C. Wu).

https://doi.org/10.1016/j.ensm.2018.06.022
Received 27 February 2018; Received in revised form 20 June 2018; Accepted 22 June 2018
Available online 22 June 2018

to better stability (higher surface energy) and faster diffusion over the surface layer (surface diffusion barrier is 0.03–0.15 eV for adatoms) [40]. Compared with Li_2CO_3, which is the main ingredient in native SEI film, Li halides is beneficial to make for a dendrite-free surface due to lower surface diffusion barriers [22,45,46].

LiF-rich artificial solid electrolyte interface (SEI) film has been verified to be a useful strategy to restrain dendrite growth in LMBs. Choudhury et al. have pointed out the importance of LiF as electrolyte additives to improve the depositional morphology during electrodeposition process [21]. Ozhabes et al. underscored the effect of LiF on controlling the surface diffusion of metal ions [45]. Zhang et al. constructed LiF-rich SEI film, which guided the Li deposit into a columnar structure [9]. These results attributed from the diffusion rate of Li^+ over a LiF surface is more than 30 times faster than Li_2CO_3, because the energy barrier for Li^+ transport over a LiF-rich surface is 0.09 eV lower than that of Li_2CO_3 [21].

Inspired by the advantages of LiF surface, we proposed to form a LiF host with good Li^+ diffusivity and chemical stability to restrain dendrite growth and prolong cycle life of LMBs. Ammonium hydrogen difluoride (NH_4HF_2) is usually used to induce fluorination of mineral raw materials to modify the mechanical properties and solubility [47–50]. Compared with many other fluoride sources, NH_4HF_2 has the advantages of good solubility and low cost [47], which has never been applied to Li metal anode modification according to the best of our knowledge. Therefore, we screen out NH_4HF_2 as the fluoride source to modify Li anode surface, which can change the chemical component and structure of Li metal anode simultaneously. The LiF-rich Li is obtained by the direct contact of fresh Li with NH_4HF_2-dimethyl sulfoxide (DMSO) solution. As the plating process progresses, Li deposits from the bottom to the top of LiF host and finally cover the surface of LiF-rich Li anode with flat and homogeneous morphology, which owing to the porous framework and low diffusion barrier in LiF. Additionally, after the depositing of 2 mA h cm^{-2}, 5 mA h cm^{-2} and 10 mA h cm^{-2} Li at 1.0 mA cm^{-2}, the scaly morphology of Li is gradually observed on the modified electrode surface.

2. Results and discussion

An artificial LiF host is formed on the surface of Li anode by the reaction of NH_4HF_2 with Li metal. To obtain the expectant LiF coated Li metal anode, high purity DMSO (> 99.9%) and suitable reaction time are necessary, if not, a layer of undesirable black substance (which is LiOH as confirmed in Fig. S1) will form on the surface of bare Li metal. We testify the feasibility of the reaction between NH_4HF_2 and Li metal to form LiF at room temperature by using density functional theoretical (DFT) method. As shown in Fig. 1, the Gibbs free energy (ΔG) of the reaction (NH_4HF_2+Li → LiF+NH_4F+H_2) is − 200.01 eV, which means that the NH_4HF_2 can reacts with Li metal spontaneously at room temperature along with the generation of LiF and small amount of hydrogen. The concentration (9.1 mg kg^{-1}) of Li in the solution after reaction is detected by inductively coupled plasma optical emission spectrometer (ICP-OES) method. The concentration value ranges from zero (before reaction) to 9.1 mg kg^{-1} (after reaction) can further prove the feasibility of the reaction. The reaction conditions, including reaction time and solution concentration have an effect on the morphology and thickness of LiF, the optimal conditions (solution concentration = 0.8 wt%, reaction time = 24 h) are filtered through a series of comparative experiments (Fig. S2). These results suggest that the LiF host is thicker, the Li^+ is harder to transport through the electronic insulated LiF. In addition, when the reaction time is shorter or the solution concentration is smaller, the shape of LiF particles will become more irregular compared with the optimized one, and thus may disturb the Li^+ diffusion path.

To confirm the components of LiF host, X-ray photoelectron spectroscopy (XPS) and X-ray Diffraction (XRD) measurements are employed to analyze the element content and valence on the surface of LiF-rich Li anode respectively. As shown in Fig. 2**(a)**, a high F content of 33.04% is achieved in the LiF host. There are a single Li 1s peak at 55.77 eV (Fig. 2**a**) and a single F 1s peak at 684.50 eV (Fig. 2**b**), which corresponding to the presence of LiF. Meanwhile, extremely low percentage of oxygen and carbon are detected due to the contamination of air during data acquisition. The XRD pattern shows three distinct peaks (Fig. 2**c**), the one at 65.3° is indexed as LiF (PDF# 45-1460), confirming the crystalline nature of the coating; the one at 36.1° is indexed as Li (PDF# 89-3940) and the weak peak at 52.5° is indexed as Li_2O_2 [45]. When compared with the bare Li anode, the LiF-rich one is gray and less metallic luster **(**Fig. 2**d).** After exposed to the air after 40 min, the bare Li anode was corroded to black tarnish, which can be attributed to oxidation of air. However, the LiF-rich one still maintained its fresh state. These results indicate that the LiF host effectively prevented the lithium from the corrosion in the atmospheric condition.

The SEM is employed to investigate the morphology of LiF on Li anode as shown in Fig. 3. The surface of LiF-rich Li is distributed with cuboid LiF particles (Fig. 3**a**). The partial enlarged morphology in Fig. 3**b** shows that the size of the particles is nonuniform but the shape is regular cuboid. As shown in Fig. 3**c**, the fluoride is uniformly covered on the surface of cuboid particles. Compared with the nonuniform distribution of Li_2CO_3 in native SEI film [51], the LiF host contributes to a phase-uniform surface on Li anode. Fig. 3**d** is the cross-sectional SEM image of LiF host, which shows a porous artificial layer full of cuboid particles. The pores are caused by the generation of hydrogen during sample preparation. The thickness of the LiF host is around 77.4 μm and the fluorine is uniformly distributed as shown in corresponding EDS image (Fig. 3**f**). The LiF host is thicker than previous similar works, but the porous structure may provide Li metal more space for Li deposition.

Ether-based electrolyte (DOL:DME-LiTFSI) has exhibited good stability with metallic lithium, particularly in the presence of $LiNO_3$ [21]. We assembled Li|Li symmetric cells without additives to effectively evaluate the morphology of Li anodes in LMBs. At 1.0 mA cm^{-2}/ 1.0 mA h cm^{-2}, both the Li| DME:DOL-LiTFSI|Li and LiF-rich Li| DME:DOL-LiTFSI|LiF-rich Li cells are disassembled to be characterized after the initial charging. The depositional morphology on bare Li anode and LiF-rich Li anode are totally different (as shown in Figs. 4**a and** 4**b)**. The SEM images illustrated that Li deposits on bare Li tend to gather at one point and form pinpoint-like Li nucleation sites. The

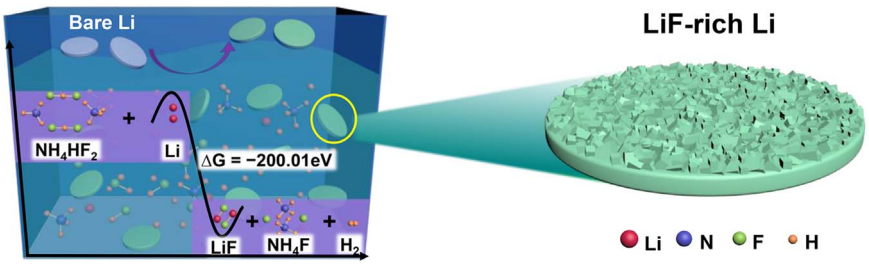

Fig. 1. Schematic diagrams of surface LiF coating and major chemical reaction. Schematic showing the surface treatment of Li metal with NH_4HF_2 and proposed major chemical reaction testified by density functional theoretical (DFT) method.

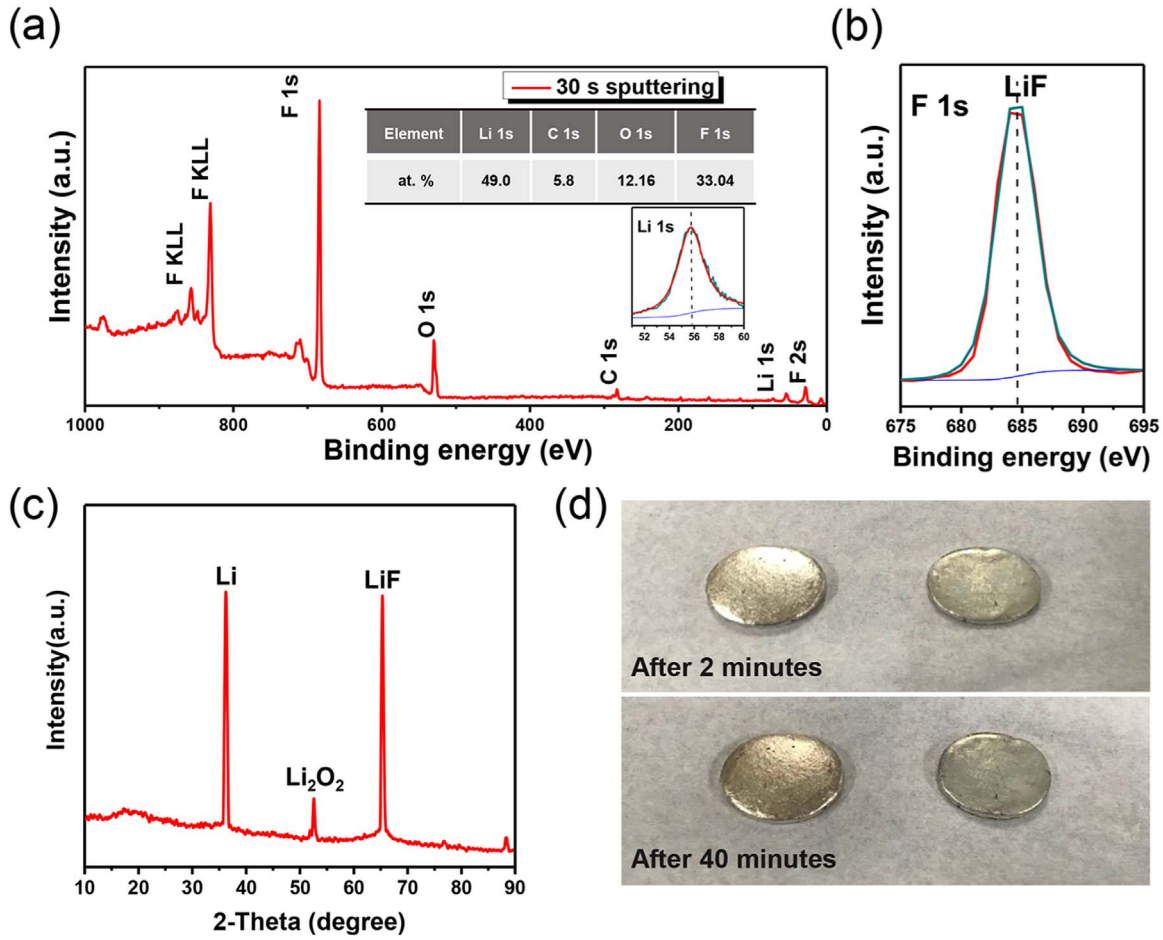

Fig. 2. (a) XPS spectrum of the LiF-coated Li anode, 30 s sputtering was performed to eliminate the air contamination, the inset table: atomic ratio of elements in the LiF host. The inset plot: XPS spectrum of Li 1s. (b) XPS spectrum of F 1s corresponding to (a). (c) XRD pattern of LiF-coated surface. (d) The photographs of bare Li anode (left) and LiF-rich Li anode (right). Exposed to the air after 2 min (up) and 40 min (bottom).

apex of each sites glitter as metallic sheen, which demonstrated the inhomogeneity of deposition. During the Li plating, Li^+ is preferentially attracted by existing nucleation sites, which possibly leads to charge accumulation and then results in Li growing into pinpoint-like bump. In contrast, the deposited Li on the LiF-rich Li anode possesses a flat wafer uniformly distributed surface. Figs. 4**c** and 4**d** are the partial magnified images for better comparison. To evaluate the effect of electrolyte on modified Li anode, the LiF-rich Li is immersed into 1 M

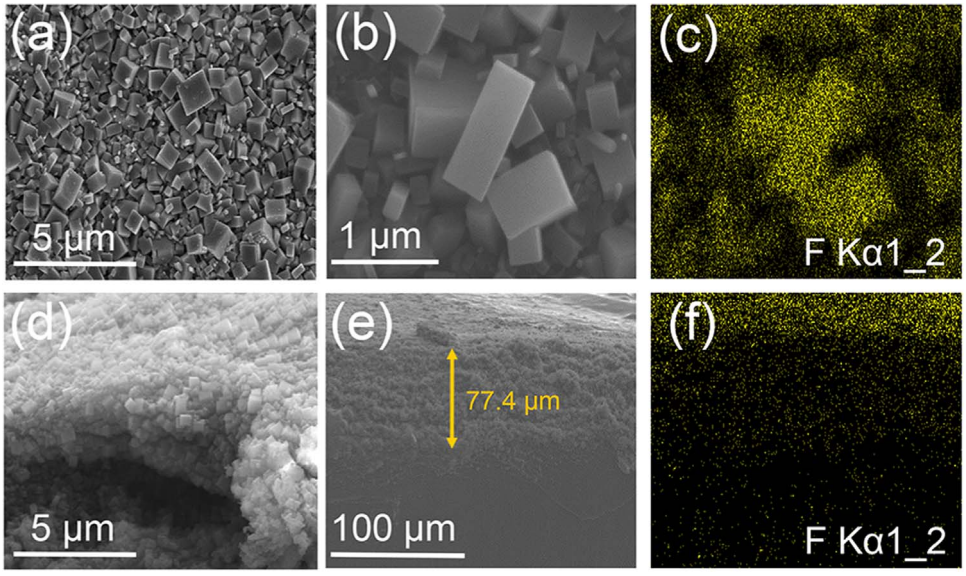

Fig. 3. Observations of the LiF on modified Li anode. Scanning electron microscopy (SEM) images showing the (a, b) surface morphology and (d, e) cross-sectional of a LiF-rich Li anode. (c, f) The corresponding elemental mapping images of the (c) surface and (f) cross section.

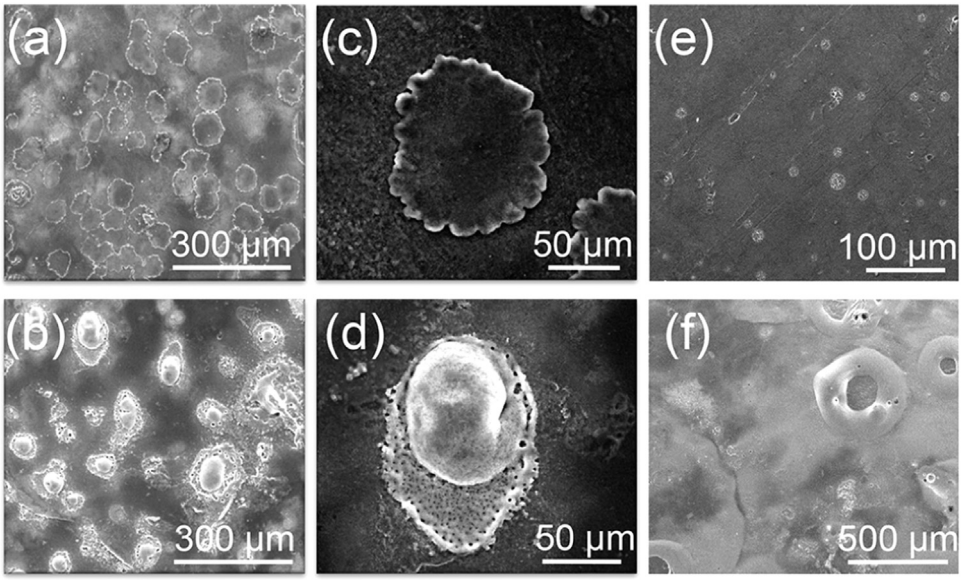

Fig. 4. The surface morphology of LiF-rich Li (a, c) and bare Li (b, d) anodes in a Li|Li symmetric cell after the initial charging. (c, d) Partial enlarged details corresponding to LiF-rich Li and bare Li anodes respectively. (e) LiF-rich Li anode immersed into 1 M LiTFSI and DME/DOL (1:1 in volume) electrolyte for 12 h. (f) LiF-rich Li anode after the first discharging.

LiTFSI and DME/DOL (1:1 in volume) electrolyte for 12 hours, after drying for 2 hours in vacuum, we find that the surface of LiF-rich Li is corroded and has circular corrosion spots (Fig. 4**e**) corresponding to the shape of deposited Li after the initial charging. The morphology of LiF-rich Li surface after the initial discharging (Fig. 4**f**) shows that stomata-like stripping sites are formed on the LiF-rich Li surface, meanwhile the mellow edge of the "stomata" greatly decrease the impact of "tip effect" in the subsequent plating process.

On bare Li anode, the inhomogeneous surface morphology and composition lead to inhomogeneous charge transfer at the electrode surface [52]. Thus, the Li metal tend to deposit on one site. In order to understand the depositional mechanism on LiF-rich Li anode, several symmetric cells are operated under 0.1 mA cm^{-2} with the cycling capacity of 0.1, 0.5, 0.7 and 1.0 mA h cm^{-2} respectively (Fig. S3). With increasing cycling capacity (Fig. S3**(a–d)**), less and shallower cuboid particles are exposed. The corresponding elemental mapping images show the cuboid particles are pristine LiF particles. In addition, the elemental composition analysis of the melanocratic ravines from energy dispersive X-ray spectroscopy (EDX) suggests the existence of a spot of O and F. The XPS analysis (Fig. S4) on modified Li anode after charging with 10 mA h cm^{-2} further confirmed that the depositional substance is lithium. Therefore, we propose the depositional mechanism as shown in Fig. 5. Compared with other LiF-modified anode, the LiF-rich anode in this work includes wealth pores, which can provide sufficient space for Li plating. Once the Li deposits initiates, it would grow continuously from the bottom gap to the top of the LiF host and finally cover the surface of the modified anode after further deposition. Additionally, the LiF results in ion distribute along with the surface of cuboid, the lateral mobility of Li^+ over a LiF surface is over 30 times larger than the original component as discussed before. So the Li metal will deposit as oblate wafer on the modified anode. Therefore, the dispersive Li^+ transportation paths would enable stable and dendrite-free electrodeposition.

Electrochemical tests are performed to evaluate the hypothesis that LiF-rich Li anode yield LMBs with long cycling stability and less possibility of failure stemmed from short-circuit. The Li|Li symmetric cells are charged and discharged at a range of current densities. Fig. 6 shows the voltage profiles as a function of time for batteries with bare Li anode and LiF-rich Li anode at current densities of 1.0, 2.0 and 5.0 mA cm^{-2} with the cycling capacity of 1 mA h cm^{-2}. As shown in Fig. 6**a**, at the current density of 1 mA cm^{-2}, the cell with LiF-rich Li anode enabled stable cycling for 520 h with a low voltage hysteresis (43.4 mV at initial cycle and 81.6 mV at the 250th cycle). Though the cells with bare Li anode shows comparable overpotential with the modified cells in the first several cycles. After 75 cycles, the overpotential of the bare Li metal cells increases considerably (> 50 mV), while the overpotential of the LiF-rich Li metal cells is stable with a tiny increase. The difference in cycling stability becomes more distinct with the increase of current density. The overpotentials for LiF-rich Li metal cells remain stable within 400 hours at current density of 2.0 and 5.0 mA cm^{-2}, while the overpotential of bare Li metal cells increases sharply (Fig. 6**b**) or displays very high overpotential **(**Fig. 6**c)**. These results suggest that

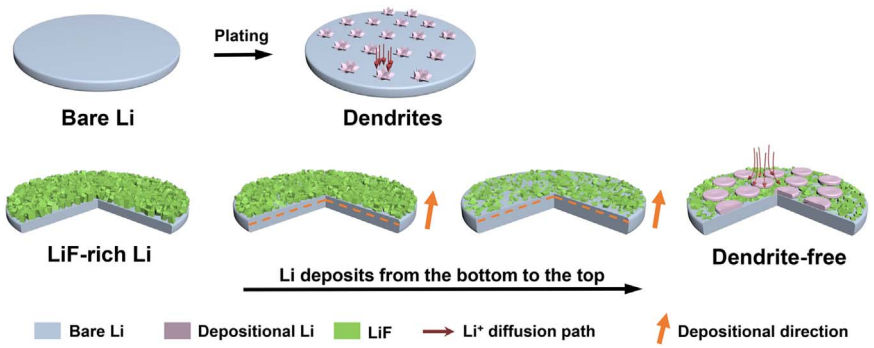

Fig. 5. The inferred electrodeposition mechanism: Lithium diffusion near the surface of electrodes represented by kermesinus arrows. LiF host is shown in green. Due to lower diffusion barrier on LiF, wafer-like Li deposition is expected, while in usual SEI, needle-like Li plating is formed.

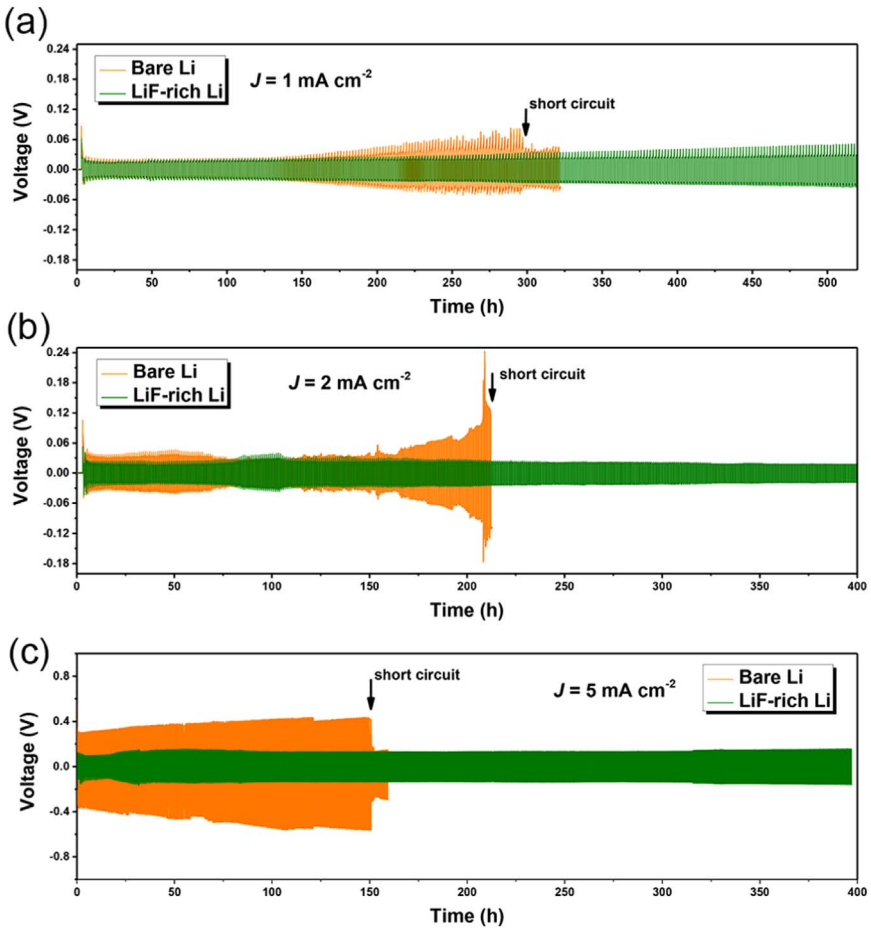

Fig. 6. Electrochemical characterization of LiF-rich Li anode. A comparison of the cycling stability of the symmetric LiF-rich Li anode (green) and bare Li anode (yellow) cells at a current density of (a) 1.0 mA cm^{-2}, (b) 2.0 mA cm^{-2}, and (c) 5.0 mA cm^{-2}, respectively.

the fast ion transport of LiF may enable the excellent cycling performance at high current densities.

The utilization of Li during repeated plating and stripping processes is numerically indicated by the Coulombic efficiency (CE) of Li|Cu half cells. The CE of Li|Cu cell has been evaluated based on the Method 3 proposed by Zhang and co-workers[53]. An average CE of the cell with LiF-rich Li anode reaches 98.5% at a current density of 1.0 mA cm^{-2}, which is much higher than that with bare Li anode at 91.07%. It's clear that the LiF host enables a stable SEI formation and flat electrodeposition, and hence effectively improve the CE compared with the control cells. A full cell is constructed from the bare Li anode and $LiFePO_4$ cathode to investigate the practical viability of LiF as a lithium host for LMBs. As shown in Fig. 7**b**, the profile at 1 mA cm^{-2} obtained from galvanostatic measurements for Li|EC:DMC-$LiPF_6$|$LiFePO_4$ and LiF-rich Li|EC:DMC-$LiPF_6$|$LiFePO_4$ respectively. Both of the cells show CE of ≈ 99% which can be attributed to the reservoir of virtually infinite lithium at anode [22]. The CE of the cell with LiF-modified anode in the initial cycles is higher than that with bare Li anode, which demonstrates that the stability of LiF host in electrolyte and the kinetics of the full cell is significantly improved by the artificial LiF host. The initial discharge specific capacity of LiF-rich Li anode is also higher than the control cell, and the descending slop of the control cell is steep during the first dozens of cycles as a result of the reduced hysteresis using LiF-rich Li as an anode. In addition, the LiF host supports the efficient surface passivation and the homogenized ion flux. Electrochemical impedance spectroscopy (EIS) measurement is performed on the symmetric cell to evaluate the interfacial resistance for both bare Li and LiF-rich Li anodes, as shown in Fig. 7**c**, where the resistance of SEI formed on LiF-rich Li (148 Ω) is smaller than that on bare Li (225 Ω) after the 1st cycle. This can be attributed to the role of LiF in decreasing SEI resistance and the increased specific surface area of cuboid LiF particles. When the same current density is applied, the increased surface area can improve the electrochemical reaction and decrease the polarization of the electrodes [54]. Therefore, the polarization between the charge and discharge plateaus for the LiF-rich Li cell is lower than that for the bare Li metal cell (Fig. 7**(d)**). It's evident that the performance of the full cell is significantly improved by the artificial LiF host.

The better cycling stability of the batteries with LiF-rich anode is on account of the stable Li/electrolyte interface, thus, to evaluate the morphology of Li anode after long-term cycling in the LMBs and provide more intuitive evidences for the aforementioned traits of LiF-rich Li anode, SEM images are obtained from galvanostatic measurements for Li|Li and LiF-rich Li|LiF-rich Li coin cells after 100 cycles respectively (Fig. 8). It is seen that the lithium depositional morphology obtained by using bare Li as electrodes are uneven and full of pinpoint-like lithium particles (Fig. 8**a**), while for the LiF-rich Li electrodes, the Li deposition is significantly smooth (Fig. 8**b**). With the magnification increases, the pinpoint-like depositional Li as shown in Fig. 8c is the same as Fig. 4d shows and the morphology of the bottom depositional Li is needle-like which indicates that during Li plating and stripping, Li tends to deposit on existing nucleation sites and then form uneven surface. In sharp contrast, the whole surface of LiF-rich Li anode is definitely oblate (Fig. 8**d**). Fig. 8**f** shows the edge of Li deposition layer, which is laminated and like squashed snow. Combined with the wafer-like uniform deposition in the initial charging process in Fig. 4c, it can be speculated that the LiF-rich host speeds up the ions diffusivity and helps Li more uniform deposit in each cycle.

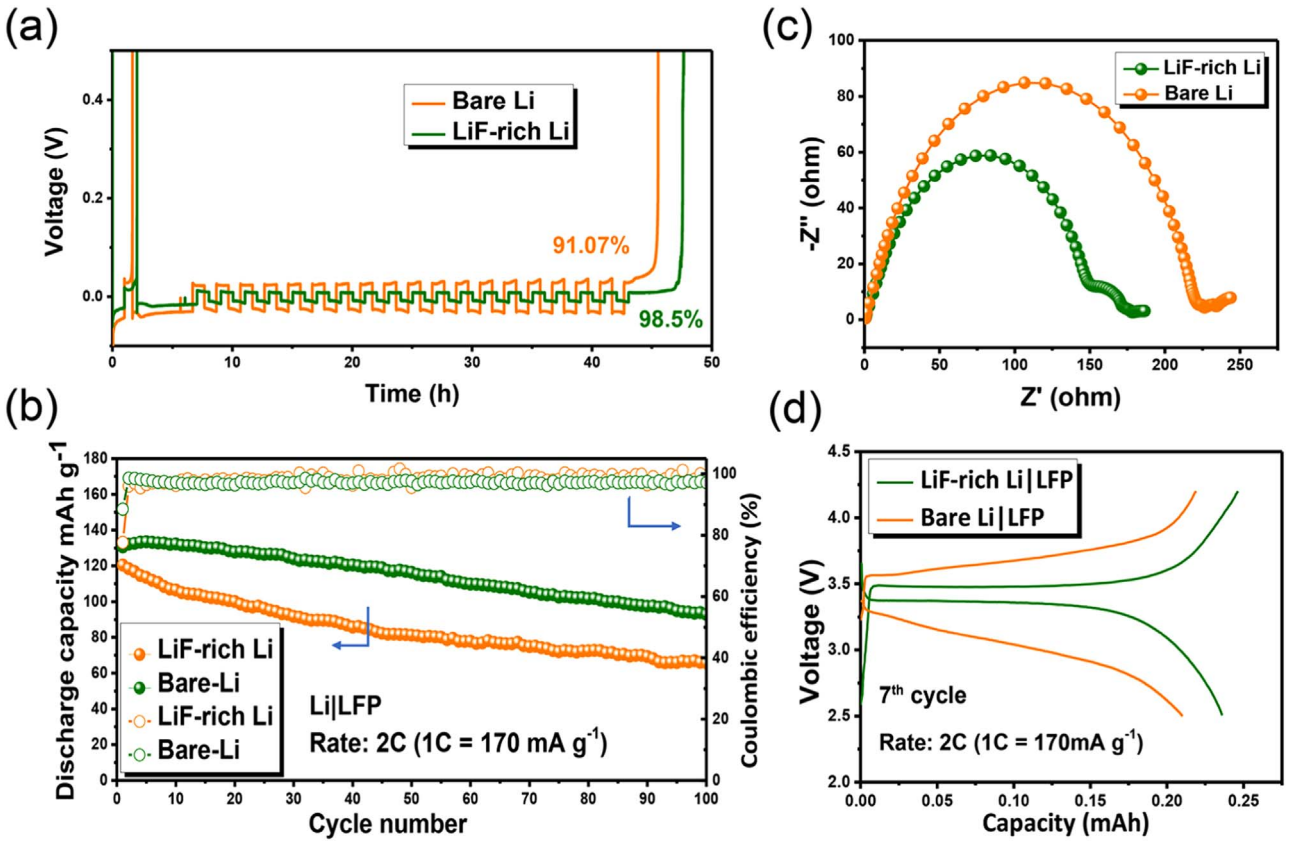

Fig. 7. (a) The voltage versus time plot in CE evaluation test. (b) Cycling performance of the Li|$LiFePO_4$ battery system using bare Li metal and LiF-rich Li anodes at a current rate of 2 C. (c) electrochemical impedance spectra (EIS) of Li|Li cells after the 1st cycle. (d) Galvanostatic profiles of Li|LFP (orange) and LiF-rich Li|LFP (green) full cells at current rate of 2 C.

The depositional conditions with different cycling capacity are also analyzed as Fig. 9 shows. With the cycling capacity achieve 2 mA h cm^{-2} (Figs. 9**a**), 5 mA h cm^{-2} (Fig. 9**b**) and 10 mA h cm^{-2} (Fig. 9**c**), the deposition morphology still remains oblate and dendrite-free. Particularly, when the cycling capacity up to 10 mA h cm^{-2}, the Li metal tends to deposit into scales as shown in Fig. 9c. The thickness of deposited Li on LiF-rich Li is much thinner than that on bare Li, which indicates that plenty of Li deposit into the gaps of porous LiF host as illustrated in Fig. S5. Additionally, with increasing cycling capacities, the thickness of remaining LiF host decreases, as shown in Fig. S6. Based on these evidences, we determine that under the influence of LiF host, the Li^+ diffusion path is homogeneous and the Li deposits from the bottom gaps to the top of LiF host, and then results in the surface of Li anode covered by lithium scales. The landform displays that the original shape of cuboid particles is unwounded, where the deposited Li has come off naturally when cut into small pieces for SEM characterization, as shown in Fig. 9**d**, which indicates the excellent stability of LiF in working batteries.

Compared with the reported strategies to restrain lithium dendrite growth, our results demonstrate a simple and innovative method to suppress lithium dendrite growth by inducing the formation of an artificial cuboid LiF host on bare Li surface. LiF has been confirmed to

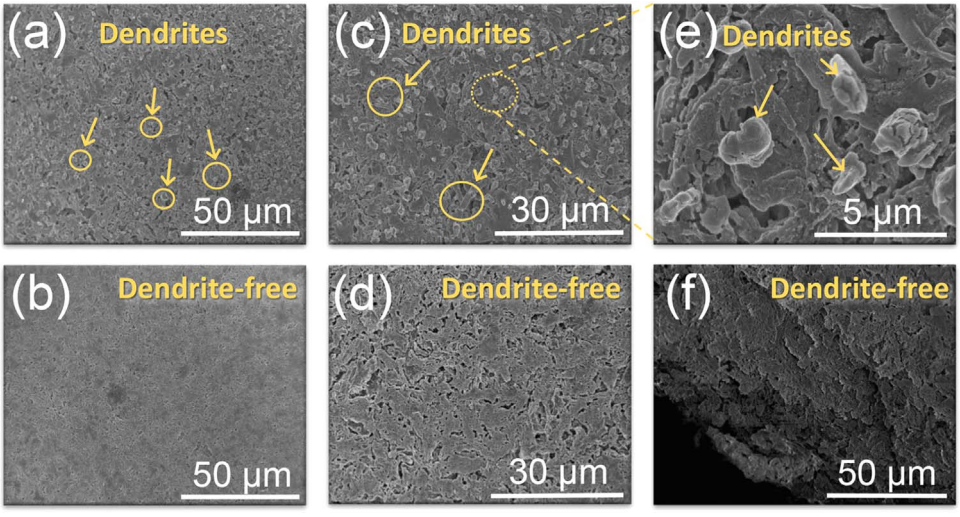

Fig. 8. The SEM images of the surface morphology of bare Li (a, c, e) and LiF-rich Li (b, d) anodes in Li|Li symmetric cells at 1.0 mA cm^{-2} with a cycling capacity of 1.0 mA h cm^{-2} after 100 cycles. (f) the edge of LiF-rich Li anode shows the Li deposition is laminated.

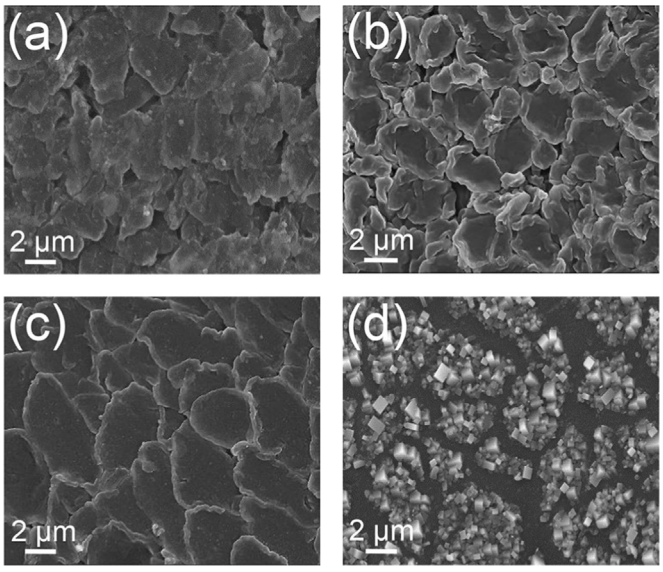

Fig. 9. The SEM images of the surface morphology of LiF-rich Li anodes in Li|Li symmetric cells at 1.0 mA cm^{-2} with a cycling capacity of (a) 2.0 mA h cm^{-2}, (b) 5.0 mA h cm^{-2}, and (c, d) 10.0 mA h cm^{-2}.

be an effective component in SEI film for dendrite suppression [26,55–57]. Our method possesses following remarkable advantages: (1) This work changed the chemical component and structure of lithium metal anode simultaneously. (2) Lithium deposits on LiF-rich Li anode is dendrite-free, though the cycling capacity up to 10 mA h cm^{-2}. (3) Excellent chemical stability of LiF host. (4) The treatment method is simple and low-cost, benefiting easy handling and scaling-up. Lithium-halide SEI layers have both high surface energy and surface mobility which are desirable properties for suppressing dendrite growth on lithium anode [58]. Among all the lithium-halide binary salts, LiF has the highest diffusion barrier but a long time to short circuit may be due to the most stable surface. Our work exemplified using a one-step method to prepare a lithium metal anode which possesses LiF and high surface area (cuboid morphology) simultaneously. It will make a difference on Li plating and battery performance if the morphology of LiF can be optimized by adjusting the reaction conditions, like temperature.

3. Conclusions

In conclusion, we fabricated a porous LiF host on bare Li metal by a facile and low-cost surface fluorination process. The rationality behind this approach is attributed to the density functional theoretical (DFT) method. The LiF host not only serves as a chemically stable interfacial layer for Li anodes by remitting corrosion reactions with electrolyte, but the abundant of pores in LiF host can guide Li grow from bottom gaps to the top and then deposit into a flat and scale-like morphology. In addition, the cuboid structure results in lower interfacial impedance. As thus, such a modified LMB displayed stable cycling over 520 h and more than 98.5% Coulombic efficiency at the current density of 1.0 mA cm^{-2} with 1.0 mA h cm^{-2}. Therefore, this surface fluorination method not only can help prepare LiF, but also shed a new light on control the surface structure of Li anode. All these features of this strategy make it a viable option for practical applications.

4. Experimental section

In this work, all the chemicals were analytical grade and without further purification. To assemble Li|$LiFePO_4$ full cells, the $LiFePO_4$ cathode material powder (80%), acetylene black (10%) as conductive additive, and polyvinylidene fluoride (10%) as binder in N-methyl-pyrrolidinone were mixed, and then ball milled for few hours to form a homogeneous slurry. After stirring, the slurry was coated on aluminum foil by a roll press to get a laminate. The laminate was dried in a vacuum oven at 80 °C for 24 h, and then cut into discs of diameter 11 mm. The areal density of active material is about 1.86 mg cm^{-2}. 1 M $LiPF_6$ dissolved in ethyl carbonate (EC) and diethyl carbonate (DEC) (1:1 in volume) were used as the electrolyte (a limited electrolyte of 60 μL was added into full cells), and Celgard 2400 was as the separator. Coin cells (CR2025) with lithium metal foil as counter electrodes and reference electrodes were assembled in an Ar-filled glove box (MBraun Labmaster130).

To assemble Li|Li symmetric cells and Li|Cu half cells, 1 M lithium bis(trifluoromethanesulfonyl) imide (LiTFSI) dissolved in 1,3-dioxolane (DOL)/1,2-dimethoxyethane (DME) (1:1 in volume) were used as electrolyte (a limited electrolyte of 60 μL was added into half cells). Li metal as counter electrodes and reference electrodes were assembled in an Ar-filled glove box (MBraun Labmaster130). Additionally, the LiF-rich Li anodes were also assembled into symmetric LiF-rich Li | LiF-rich Li coin cells and LiF-rich Li | Cu half cells. In a typical preparation, Li anode was scraped and polished with a sharp blade until the surface of the Li anode was extremely shiny. After polishing, the Li anode was dipped in the treating solution (0.8 wt% NH_4HF_2 in DMSO solution) for 24 h. Upon removal from the solution, excess liquid was removed using a lint-free wipe, and the sample was dried at 25 °C for 2 h under vacuum. The obtained Li anode was denoted as LiF-rich Li.

To gain insight into the Li deposition/dissolution in the Li metal battery, we disassembled the coin cells in a glove box. The anodes were washed with DME three times. After washing, the Li electrodes were dried under vacuum for 2 h to remove the residual electrolyte. The anodes were transferred for ex situ scanning electron microscopy (SEM), X-ray diffraction (XRD), and X-ray photoelectron spectroscopy (XPS) characterizations. XRD was performed on Rigaku Ultima IV-185 with Cu Kα radiation between 10 and 90° 2θ at a scan rate of 8° 2θ min^{-1}. The surface morphology of the sample was observed by field-emission scanning electron microscopy (FE-SEM) HITACHI S-4800. Energy-dispersive X-ray detector (EDX) equipped on the SEM above. The X-ray photoelectron spectrometer (XPS) was performed on PHI QUANTERA-II SXM system. Galvanostatic charge-discharge test of the electrode were performed in Land battery test system (CT2001A). Electrochemical impedance spectroscopy (EIS) measurement was carried out from 1 × 105 Hz to 0.01 Hz with an AC perturbation signal of 5 mV and conducted on a CHI 660C electrochemical workstation.

Calculations are performed using the combination of Becke's hybrid 3-Parameter exchange functional and Lee-Yang-Parr's correlation functional known as B3LYP. All the calculations are carried out with Gaussian 09 program and the result are visualized with the help of Gauss View 5.0 program. The geometries are optimized without any symmetry meanwhile the frequency analysis was performed at the same level. As there were no imaginary frequencies had found, geometries belong to the minimum of the potential energy surface. The threshold for the energy and force convergence is set to 1E−5 eV/Å and 1E−3 eV/Å. Besides, the atomic properties are represented by 6–311+G(d) basis sets.

Acknowledgements

This work was supported by the National Basic Research Program of China (Grant no. 2015CB251100).

Appendix A. Supplementary material

Supplementary data associated with this article can be found in the online version at doi:10.1016/j.ensm.2018.06.022.

References

[1] X.B. Cheng, R. Zhang, C.Z. Zhao, F. Wei, J.G. Zhang, Q. Zhang, Adv. Sci. 3 (2016) 1500213.
[2] W. Xu, J. Wang, F. Ding, X. Chen, E. Nasybulin, Y. Zhang, J.G. Zhang, Energy Environ. Sci. 7 (2014) 513–537.
[3] M. Armand, J.M. Tarascon, Nature 451 (2008) 652–657.
[4] S. Chu, Y. Cui, N. Liu, Nat. Mater. 16 (2016) 16–22.
[5] H.J. Peng, J.Q. Huang, Q. Zhang, Chem. Soc. Rev. 46 (2017) 5237–5288.
[6] F. Wu, C. Wu, Chin. Sci. Bull. 59 (2014) 3369–3376.
[7] H. Wang, Y. Bai, S. Chen, F. Wu, C. Wu, Prog. Chem. 25 (2013) 1392–1400.
[8] S. Gu, H. Wang, C. Wu, Y. Bai, H. Li, F. Wu, Energy Storage Mater. 6 (2017) 9–17.
[9] X.Q. Zhang, X. Chen, R. Xu, X.B. Cheng, H.J. Peng, R. Zhang, J.Q. Huang, Q. Zhang, Angew. Chem. 129 (2017) 14395–14399.
[10] X.B. Cheng, R. Zhang, C.Z. Zhao, Q. Zhang, Chem. Rev. 117 (2017) 10403–10473.
[11] J.B. Goodenough, K.S. Park, J. Am. Chem. Soc. 135 (2013) 1167–1176.
[12] Y. Guo, H. Li, T. Zhai, Adv. Mater. 29 (2017) 1700007.
[13] L. Fan, H.L. Zhuang, L. Gao, Y. Lu, L.A. Archer, J. Mater. Chem. A 5 (2017) 3483–3492.
[14] T. Liu, M. Leskes, W. Yu, A.J. Moore, L. Zhou, P.M. Bayley, G. Kim, C.P. Grey, Science 350 (2015) 530–533.
[15] Z. Zhang, Q. Zhang, Y. Chen, J. Bao, X. Zhou, Z. Xie, J. Wei, Z. Zhou, Angew. Chem. 54 (2015) 6550–6553.
[16] Z. Wang, Z. Liang, W.L. Xiong, Adv. Mater. 43 (2012) 1903–1911.
[17] H. Li, C. Wu, F. Wu, Y. Bai, Rare Met. Mater. Eng. 43 (2014) 1525–1530.
[18] X. Shen, H. Liu, X.B. Cheng, C. Yan, J.Q. Huang, Energy Storage Mater. 12 (2018) 161–175.
[19] N.W. Li, Y.X. Yin, J.Y. Li, C.H. Zhang, Y.G. Guo, Adv. Sci. 4 (2016) 1600400.
[20] J. Qian, W. Xu, P. Bhattacharya, M. Engelhard, W.A. Henderson, Y. Zhang, J.G. Zhang, Nano Energy 15 (2015) 135–144.
[21] S. Choudhury, L.A. Archer, Adv. Electron. Mater. 2 (2016) 1500246.
[22] X.Q. Zhang, X.B. Cheng, X. Chen, C. Yan, Q. Zhang, Adv. Funct. Mater. 27 (2017) 1605989.
[23] F. Ding, W. Xu, G.L. Graff, J. Zhang, M.L. Sushko, X. Chen, Y. Shao, M.H. Engelhard, Z. Nie, J. Xiao, X. Liu, P.V. Sushko, J. Liu, J.G. Zhang, J. Am. Chem. Soc. 135 (2013) 4450–4456.
[24] Y. Zhang, J. Qian, W. Xu, S.M. Russell, X. Chen, E. Nasybulin, P. Bhattacharya, M.H. Engelhard, D. Mei, R. Cao, F. Ding, A.V. Cresce, K. Xu, J.G. Zhang, Nano Lett. 14 (2014) 6889–6896.
[25] F. Ding, W. Xu, X. Chen, J. Zhang, Y. Shao, M.H. Engelhard, Y. Zhang, T.A. Blake, G.L. Graff, X. Liu, J.G. Zhang, J. Phys. Chem. C 118 (2014) 4043–4049.
[26] R. Miao, J. Yang, Z. Xu, J. Wang, Y. Nuli, L. Sun, Sci. Rep. 6 (2016) 21771.
[27] X.X. Zeng, Y.X. Yin, Y. Shi, X.D. Zhang, H.R. Yao, R. Wen, X.W. Wu, Y.G. Guo, Chemistry 4 (2018) 298–307.
[28] Y. Liu, D. Lin, Y. Jin, K. Liu, X. Tao, Q. Zhang, X. Zhang, Y. Cui, Sci. Adv. 3 (2017) eaao0713.
[29] C.Z. Zhao, X.Q. Zhang, X.B. Cheng, R. Zhang, R. Xu, P.Y. Chen, H.J. Peng, J.Q. Huang, Q. Zhang, Proc. Natl. Acad. Sci. USA 114 (2017) 11069–11074.
[30] H. Wan, G. Peng, X. Yao, J. Yang, P. Cui, X. Xu, Energy Storage Mater. 4 (2016) 59–65.
[31] D. Hui, Y.X. Yin, X.X. Zeng, J.Y. Li, J.L. Shi, Y. Shi, R. Wen, Y.G. Guo, L.J. Wan, D. Hui, Energy Storage Mater. 10 (2017) 85–91.
[32] K.K. Fu, Y. Gong, J. Dai, A. Gong, X. Han, Y. Yao, C. Wang, Y. Wang, Y. Chen, C. Yan, Y. Li, E.D. Wachsman, L. Hu, Proc. Natl. Acad. Sci. USA 113 (2016) 7094–7099.
[33] K.K. Fu, Y. Gong, B. Liu, Y. Zhu, S. Xu, Y. Yao, W. Luo, C. Wang, S.D. Lacey, J. Dai, Y. Chen, Y. Mo, E.D. Wachsman, L. Hu, Sci. Adv. 3 (2017) e1601659.
[34] W. Luo, Y. Gong, Y. Zhu, Y. Li, Y. Yao, Y. Zhang, K.K. Fu, G. Pastel, C.F. Lin, Y. Mo, E.D. Wachsman, L. Hu, Adv. Mater. 29 (2017) 1606042.
[35] Y.Z. Sun, J.Q. Huang, C.Z. Zhao, Q. Zhang, Sci. Chin. Chem. 60 (2017) 1508–1526.
[36] X. Han, Y. Gong, K. Fu, X. He, G.T. Hitz, J. Dai, A. Pearse, B. Liu, H. Wang, G. Rubloff, Nat. Mater. 16 (2017) 572–579.
[37] W.D. Richards, L.J. Miara, Y. Wang, J.C. Kim, G. Ceder, Chem. Mater. 28 (2015) 266–273.
[38] R. Zhang, X.R. Chen, X. Chen, X.B. Cheng, X.Q. Zhang, C. Yan, Q. Zhang, Angew. Chem. Int. Ed. 56 (2017) 7764–7768.
[39] A. Pei, G. Zheng, F. Shi, Y. Li, Y. Cui, Nano Lett. 17 (2017) 1132–1139.
[40] L. Wang, L. Zhang, Q. Wang, W. Li, B. Wu, W. Jia, Y. Wang, J. Li, H. Li, Energy Storage Mater. 10 (2017) 16–23.
[41] Q. Li, F.L. Zeng, Y.P. Guan, Z.Q. Jin, Y.Q. Huang, M. Yao, W.K. Wang, A.B. Wang, Energy Storage Mater. 13 (2018) 151–159.
[42] X.B. Cheng, C. Yan, X. Chen, C. Guan, J.Q. Huang, H.J. Peng, R. Zhang, S.T. Yang, Q. Zhang, Chemistry 2 (2017) 258–270.
[43] N.W. Li, Y. Shi, Y.X. Yin, X.X. Zeng, J.Y. Li, C.J. Li, L.J. Wan, R. Wen, Y.G. Guo, Angew. Chem. Int. Ed. 57 (2018) 1505–1509.
[44] F. Wu, N. Zhu, Y. Bai, Y. Gao, C. Wu, Green. Energy Environ. 3 (2018) 71–77.
[45] Y. Ozhabes, D. Gunceler, T. Arias, arXiv:1504.05799v1.
[46] Y. Lu, S. Gu, X. Hong, K. Rui, X. Huang, J. Jin, C. Chen, J. Yang, Z. Wen, Energy Storage Mater. 11 (2017) 16–23.
[47] V. Geetha, G. Buvaneswari, Mater. Res. Bull. 45 (2010) 1866–1870.
[48] A.I. Khanchuk, V.P. Molchanov, M.A. Medkov, D.G. Epov, G.F. Krysenko, M.G. Blokhin, E.V. Elovsky, Dokl. Chem. 460 (2015) 29–32.
[49] I.G. Maslennikova, Russ. J. Appl. Chem. 82 (2009) 1333–1337.
[50] Y. Bai, X. Zhou, C. Zhan, L. Ma, Y. Yuan, C. Wu, M. Chen, G. Chen, Q. Ni, F. Wu, R. Shahbazian-Yassar, T. Wu, J. Lu, K. Amine, Nano Energy 32 (2017) 10–18.
[51] N.W. Li, Y.X. Yin, C.P. Yang, Y.G. Guo, Adv. Mater. 28 (2016) 1853–1858.
[52] M.H. Ryou, Y.M. Lee, Y. Lee, M. Winter, P. Bieker, Adv. Funct. Mater. 25 (2015) 834–841.
[53] B.D. Adams, J. Zheng, X. Ren, W. Xu, J.G. Zhang, Adv. Energy Mater. 8 (2018) 1702097.
[54] J. Heine, S. Krüger, C. Hartnig, U. Wietelmann, M. Winter, P. Bieker, Adv. Energy Mater. 4 (2013) 1300815.
[55] Z. Jie, L. Lei, F. Shi, T. Lei, G. Chen, A. Pei, S. Jie, Y. Kai, G. Zhou, X. Jin, J. Am. Chem. Soc. 139 (2017) 11550–11558.
[56] D. Lin, Y. Liu, W. Chen, G. Zhou, K. Liu, B. Dunn, Y. Cui, Nano Lett. 17 (2017) 3731–3737.
[57] Y. Ma, Z. Zhou, C. Li, L. Wang, Y. Wang, X. Cheng, P. Zuo, C. Du, H. Huo, Y. Gao, Energy Storage Mater. 11 (2017) 197–204.
[58] Y. Lu, Z. Tu, L.A. Archer, Nat. Mater. 13 (2014) 961–969.

Update

Energy Storage Materials

Volume 29, Issue , August 2020, Page 386

DOI: https://doi.org/10.1016/j.ensm.2020.03.028

Energy Storage Materials 29 (2020) 386

Contents lists available at ScienceDirect

Energy Storage Materials

journal homepage: www.elsevier.com/locate/ensm

Corrigendum for "Regulating Li deposition by constructing LiF-rich host for dendrite-free lithium metal anode" [Energy Storage Mater. 16 (2019) 411-418]

Yanxia Yuan [a], Feng Wu [a,b], Ying Bai [a,**], Yu Li [a], Guanghai Chen [a], Zhaohua Wang [a], Chuan Wu [a,b,*]

[a] Beijing Key Laboratory of Environmental Science and Engineering, School of Materials Science & Engineering, Beijing Institute of Technology, Beijing, PR China
[b] Collaborative Innovation Center of Electric Vehicles in Beijing, Beijing, 100081, China

The authors regret that a label in figure 7(b) was not correctly presented, namely, the sample names of "Bare Li" and "LiF-rich Li" should be switched.

The correct figure should be revised as below:

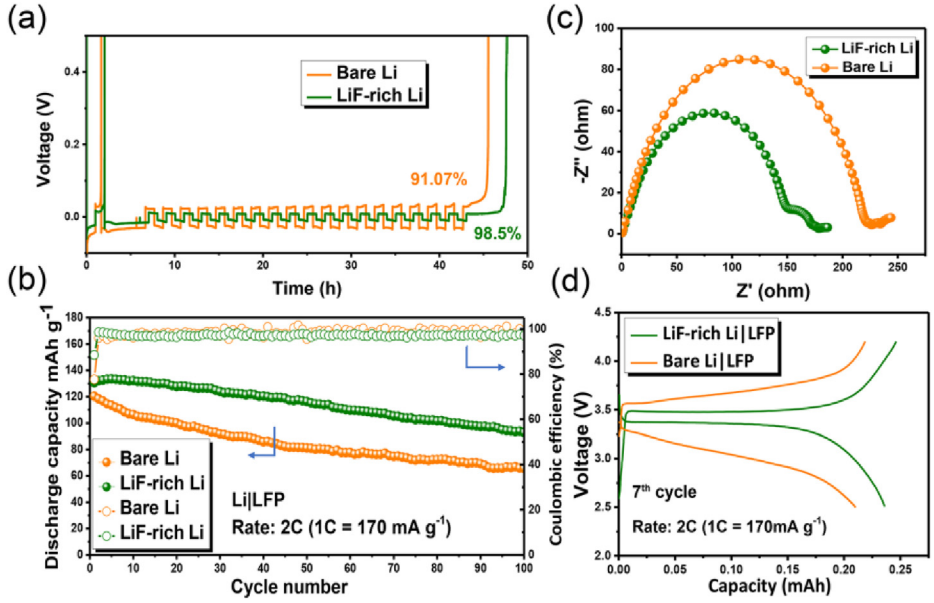

The authors would like to apologize for any inconvenience caused.

DOI of original article: https://doi.org/10.1016/j.ensm.2018.06.022.
* Corresponding author. Beijing Key Laboratory of Environmental Science and Engineering, School of Materials Science & Engineering, Beijing Institute of Technology, Beijing, PR China.
** Corresponding author.
E-mail addresses: membrane@bit.edu.cn (Y. Bai), chuanwu@bit.edu.cn (C. Wu).

https://doi.org/10.1016/j.ensm.2020.03.028

Available online 2 April 2020